The role of H_2O on the extraction of melt from crystallising magmas

Hartung, Eva; Weber, Gregor; Caricchi, Luca

How to cite

HARTUNG, Eva, WEBER, Gregor, CARICCHI, Luca. The role of H_2O on the extraction of melt from crystallising magmas. In: Earth and Planetary Science Letters, 2019, vol. 508, p. 85–96. doi: 10.1016/j.epsl.2018.12.010

This publication URL: https://archive-ouverte.unige.ch/unige:112707
Publication DOI: 10.1016/j.epsl.2018.12.010

The role of H_2O on the extraction of melt from crystallising magmas

Eva Hartung, Gregor Weber, Luca Caricchi

Department of Earth Sciences, University of Geneva, Rue des Maraîchers 13, 1205 Geneva, Switzerland

Corresponding authors:

Eva Hartung email: eva.hartung@unige.ch

Keywords: rhyolite-MELTS, silicic volcanism, water content, melt extraction, segregation timescales, Takidani pluton

ABSTRACT

The segregation and accumulation of felsic melts, from crystallising crustal magma reservoirs, is essential for the chemical evolution of the crust and is a phenomenon preceding some of the largest eruptions on Earth. The physical properties of residual melt and magma and the time over which the conditions remain appropriate for melt extraction are important factors controlling the efficiency of melt extraction and the distribution of melt in magma reservoirs. Here we focus on the initial magma H_2O content as it affects both the physical properties of the residual melt and the timescales at which conditions remain appropriate for melt extraction during progressive magma crystallisation.

We use rhyolite-MELTS simulations to evaluate the physical evolution of crystallising granodioritic (or dacitic) hydrous magma (i.e. ≥1 wt.% H_2O) at shallow depth at 200 MPa. To

constrain the solidification timescales of reservoirs containing magmas with initially different water content, we perform 2.5D thermal modelling. We combine these results with calculations of melt extraction velocity by compaction and hindered settling to identify the optimal conditions at which melt segregation occurs. These calculations suggest that hydrous felsic magmas that attain water saturation after 40 wt.% crystallisation (rheological locking point) are best suited for melt extraction. Once water-saturation is achieved, the rate of release of latent heat of crystallisation and with it the time magma spends within a given temperature interval increases while the viscosity of the residual liquid and crystal-liquid density contrast remain favourable for melt segregation. We first test our findings on the Takidani pluton (Japan) because it shows evidences of residual melt segregation from crystallising magma, and is associated with caldera-forming eruptions. We finally generalise our results to crustal magma reservoirs containing hydrous felsic magmas. Our results suggest that if segregation starts at rheological locking (i.e. crystallinity of 40-50 wt.%) upper crustal reservoirs of ≥100 km^3 granodioritic (i.e. dacitic) magma with more than 2 wt.% H_2O can produce large melt-rich caps at the top of partially crystallised magma reservoirs in few hundreds to few thousands of years. The formation of separate melt lenses becomes more likely when segregation of melt starts at crystallinities>0.6.

Our results suggest that the initial water content of magma plays an important role in modulating the distribution of eruptible melt in upper crustal reservoirs. Reservoirs of felsic and water-poor (<2wt.%) magmas tend to be associated with the formation of isolated pockets of crystal poor and eruptible magma, which could account for the often-observed geochemical heterogeneity of the products of large caldera forming eruptions in the Snake River Plane. The limited dimensions of these eruptible magma pockets make their detection by geophysical methods challenging.

1 Introduction

The accumulation and storage of viscous high-silica melt in shallow magmatic reservoirs is a process preceding some of the largest explosive eruptions on Earth. The distribution of crystal poor and eruptible lenses of magmas within highly crystallised magma reservoir cannot be resolved by geophysical methods for intrinsic limits of spatial resolution (Bedrosian et al., 2018; Huang et al., 2015). The timescale of extraction of viscous felsic melt from highly crystallised magmas are also only broadly constrained varying from months to thousands of years (Bachmann and Huber, 2018; Druitt et al., 2012; Gualda et al., 2018; Huber et al., 2012; Wilson and Charlier, 2016). Here we use a field example of extraction of felsic melt from crystallising magma, in combination with thermal modelling, to investigate the role of magma water content on the distribution and timescale of extraction of felsic melts from reservoirs of crystallising felsic magma.

Segregation of interstitial melt from a rheologically-locked partially-crystallised magma body is a potential mechanism for the accumulation of crystal-poor and eruptible rhyolite (Bachmann and Bergantz, 2004; Dufek and Bachmann, 2010; Hildreth, 2004, 1981; Hildreth and Wilson, 2007; Marsh, 1981). Thermo-mechanical simulations suggest that the efficiency of melt extraction for common hydrous silicic magma compositions is highest at crystal contents between 50% and 70% (Dufek and Bachmann, 2010). Moreover, these studies emphasise that the probability of extraction and the amount of interstitial melt segregated is not only controlled by the physical properties of residual melt and magma, but also by the time spent by magma at conditions best suited for melt extraction (Dufek and Bachmann, 2010; Huber et al., 2009). This, in turn, is a function of the ratio between the rate of heat loss and the rate of release of latent heat

of crystallisation during progressive cooling of a magma reservoir, and evolution of the physical properties of the residual melt and magma with increasing crystallinity (Caricchi and Blundy, 2015; Huber et al., 2009; Lee et al., 2015; Melekhova et al., 2013). The results of these studies permit to draw some general conclusions about extraction of residual melt in felsic systems: i) Independently of the process leading to the extraction of residual melt in crystallising felsic magmas, the separation between residual melt and crystals occurs when magma is rheologically locked (i.e. crystal fraction >0.4; (Dufek and Bachmann, 2010; Huber et al., 2010; Marsh, 1981); ii) The velocity of residual melt extraction is directly proportional to the ratio between the density difference of crystals and residual melt and the viscosity of the residual melt (Bachmann and Bergantz, 2004; Dufek and Bachmann, 2010) ; iii) The longer magma spends at conditions suitable for residual melt extraction, the larger is the amount of residual melt extracted (Dufek and Bachmann, 2010; Huber et al., 2009).

Large-scale segregation of rhyolitic melts from highly crystallised magmas is commonly inferred to precede the eruption of rhyolitic magmas (Bachmann and Bergantz, 2004; Deering et al., 2011; Hildreth and Wilson, 2007), however, evidences for such segregation processes remains scarce or obscure in the intrusive record (Coleman et al., 2004; Gelman et al., 2014; Lee et al., 2015; Vigneresse, 2014). In recent years, various studies have targeted melt extraction processes in the geological record using radiogenic isotopes (Andersen et al., 2017), whole-rock and mineral chemistry (Barnes et al., 2017; Hartung et al., 2017), and rock fabrics (Holness et al., 2017). The Takidani pluton in Central Japan shows evidence of melt segregation processes and is used here as a case study to investigate the formation of bodies of crystal-poor and eruptible melt in the upper crust (Hartung et al., 2017). This pluton has been shown to present the source of dacitic and rhyolitic volcanic eruptions (Harayama, 1992; Kimura and Nagahashi,

2007; Nagahashi et al., 2000). The pluton is texturally zoned, with a gradual transition (over about 50 m) from equigranular granodiorite to porphyritic granite (Fig. 1). Whole rock and mineral chemistry suggest that the porphyritic unit (pGT) was extracted from underlying granodiorite (GDT) once the residual melt fraction dropped to 40-50 wt.% (Figs. 1, 2a; Hartung et al., 2017). The initial water content of the granodiorite associated with melt segregation is estimated between 3 and 4 wt.% H_2O based on mineral chemistry, crystallisation sequence and relative abundance of the mineral phases (Hartung et al., 2017).

In this study, we focus on the effects of the initial water content on the timescales the magma spends at crystallinities larger than about 40 wt.%, which are considered favourable for the extraction of residual melt (Bachmann and Bergantz, 2004; Dufek and Bachmann, 2010). We first calculate the evolution with temperature and crystallinity of the physical properties of magma and residual melt for granodioritic (i.e. dacitic) magmas with water contents (H_2O_i) between 1 and 6 wt.%. The velocity of melt extraction for crystallinities between 40 and 80 wt.% are estimated using hindered settling (Davis and Acrivos, 1985) and compaction-driven segregation (McKenzie, 1984). To constrain the maximum timescales available for segregation to occur we perform thermal modelling for reservoirs of different volumes and shapes. The aims of this study are (1) to constrain the effect of H_2O_i content on the efficiency of melt extraction, (2) to identify the conditions that led to the extraction of residual melt from the Takidani pluton and estimate the timescales of this process, (3) to define the impact of H_2O_i content on the architecture of upper crustal magma reservoirs.

2 Material and methods

2.1 The Takidani Pluton: Evidences for melt segregation

In the following we provide a summary of the main results of a geochemical study previously performed on the Takidani pluton (Hartung et al., 2017), which provides the background and motivation for this study. The Takidani pluton is a well exposed and young pluton (1.6 Ma; Harayama, 1992; Ito et al., 2017), located in the Central Japan Alps. The pluton is vertically exposed over 1800 m (Harayama et al., 2003) from a tectonic contact at the base to a magmatic roof contact with older volcanic rocks (i.e. Hotaka Andesite, Harayama, 1994). Textural, chemical and isotopic evidence of large-scale melt segregation is observed in the upper part of the pluton (Figs. 1, 2; Hartung et al., 2017). The rock textures of the Takidani pluton change from holocrystalline to progressively more porphyritic appearance from the base and centre to the roof of the intrusion. Whole-rock geochemistry shows that the rocks immediately below the porphyritic unit are depleted in incompatible elements, while the porphyritic unit is enriched in incompatible elements (Fig. 1; Hartung et al., 2017). Data obtained through quantitative evaluation of minerals by QEMSCAN and electron microprobe analyses (EPMA) are used to determine the area percent and chemical composition of the matrix components (equivalent to residual melt composition) throughout the upper section of the Takidani pluton, where evidence for melt extraction is observed (Fig. 1; supplementary data: Table 1). These data show progressive enrichment in the residual melt components defined by quartz (Qtz), alkali feldspar (Kfs) and albite-rich plagioclase (Plg<An30) from the equigranular granodiorite (GDT) to the porphyritic granite (pGT; Fig. 1). The relative amounts of quartz (Qtz), albite (Ab), and orthoclase (Or) and therefore the melt compositions, however, do not change across the textural and chemical transition (Fig. 1; supplementary data: Table 1). This suggests that the residual

138 melt had a chemical composition close to the granitic minimum after emplacement at
139 approximately 200 MPa (Johannes and Holtz, 1996) and that the extraction of the residual melt,
140 now represented by the porphyritic unit, occurred once magma crystallised sufficiently for the
141 residual melt to acquire a composition close to the granitic minimum (Fig. 1). Mineral chemistry
142 provides additional support for the extraction of residual melt once the magma was rheologically
143 locked (Hartung et al., 2017).

144 Plagioclase phenocrysts in the granodioritc unit below the porphyritic have cores of
145 different chemistry that are overgrown by a distinct rim of common composition, which is
146 consistent with the composition of plagioclase in the matrix of the porphyritic unit (Hartung et
147 al., 2017). An increase in Rb (incompatible during crystallisation of the Takidani granodiorite;
148 Hartung et al., 2017) in plagioclase phenocrysts increases by more than a factor of two from the
149 core to the common outer rim. This suggest that once magma crystallised to approximately 40-50
150 wt.%, plagioclase acquired the same composition indicating rheological locking (Fig. 2). Within
151 this crystallinity range the residual melt was extracted leading to the formation of the porphyritic
152 unit of the Takidani pluton that contains matrix plagioclase with the same composition of the
153 plagioclase rims of the underlying granodioritic unit.

154 Inclusions of orthopyroxene in amphibole, amphibole thermometry, plagioclase
155 composition, and comparison with the phase equilibria experiments of Costa et al. (2004),
156 highlight that amphibole became stable once the magma achieved crystallinities of 40-50 wt.%
157 (Hartung et al., 2017). The late appearance of amphibole at low temperatures and core to rim
158 plagioclase chemistry indicate that the Takidani magma was not initially water-saturated (Costa
159 et al., 2004) and contained initially between 3 and 4 wt.% H_2O.

On the basis of the collected evidences we conclude that the pGT unit represents a lens of residual melt extracted from the underlying GDT granodiorite. The extraction of residual melt from the crystallising magma occurred after the magma became rheologically locked, at which point the residual magma had reached water saturation (Costa et al., 2004; Hartung et al., 2017). The evidence supporting initial water undersaturation of the magma and melt extraction for the Takidani pluton motivate us to investigate the role of initial water content on the extraction of felsic melt from crystallising magmas.

2.2 Rhyolite-MELTS simulations

Existing experimental data do not cover the entire range of temperature and water content required to trace the evolution of residual melt during cooling and crystallisation of magma in the upper crust (Costa et al., 2004; Holtz et al., 2005; Scaillet and Evans, 1999). Thus, we use rhyolite-MELTS (Gualda et al., 2012) to calculate the chemical and physical evolution of residual melt of dacitic (or granodioritic) magma from liquidus to near solidus temperature and over the entire range of initial water content between 1 wt.% and water saturation. Because granodiorites represent about 95 wt.% of the upper crust (Rudnick and Gao, 2003) with a composition similar to the starting material of Costa et al. (2004), we use the latter for the rhyolite-MELTS calculations. While rhyolite-MELTS it currently not capable of correctly identifying the stability of hydrous phases such as amphibole and biotite, here we use rhyolite MELTS especially to trace general evolution of residual melt chemistry and magma crystallinity. To test the performance of rhyolite-MELTS we compare the calculated residual melt compositions with residual melts produced experimentally by Costa et al. (2004) using the same starting composition. For all calculations, the confining pressure was fixed at 200 MPa, which

183 are the conditions applied in the experiments of Costa et al. (2004) and comparable to the
184 inferred emplacement depth of many granitic intrusions including the Takidani pluton (Hartung
185 et al., 2017). The oxygen fugacity was initially set to the nickel-nickel oxide buffer (NNO) to
186 calculate the liquidus temperature (for different H_2O_i), but remained unconstrained during
187 progressive heat extraction. The evolution of the residual melt chemistry as function of
188 temperature and initial water content calculated with rhyolite-MELTS is comparable to that
189 obtained in the experiments of Costa et al. (2004; Fig.3). Importantly, rhyolite-MELTS can
190 accurately reproduce the evolution of silica content of the residual melt, which together with
191 H_2O plays a dominating role in controlling the viscosity of melts (Hess and Dingwell, 1996).
192 Additionally, the decrease of melt fraction with temperature for different initial water content
193 follows paths that are comparable to those determined experimentally by Whitney (1988; Fig.
194 4b), hence we consider the rhyolite-MELTS calculations appropriate to compare the evolution of
195 physical properties of hydrous magmas during progressive crystallisation.
196 To quantify the time magma spends within different temperature interval we perform
197 rhyolite-MELTS simulations by removing an equal amount of enthalpy (i.e. 1 J g^{-1}) at constant
198 pressure from the system at each step (n) starting from the liquidus temperature down to a
199 temperature (T) of about 740°C, which corresponds to a residual melt fraction of about 0.1. If a
200 fixed amount of enthalpy is extracted from the magma during solidification, which would be
201 appropriate for quasi-eutectic magma compositions (Gualda et al., 2018), the number of
202 modelling steps within a given temperature interval becomes proportional to the time spent by
203 the magma within a given interval of temperature. This is important to be able to quantify the
204 total time that magma spends within the temperature and crystallinity range at which the
205 conditions are most conducive to melt extraction (Dufek and Bachmann, 2010). Considering that

the rate of heat loss will decrease during magma crystallisation because of the decreasing temperature difference between magma and host rocks, our approach increasingly underestimates the time spent within a given temperature range. This is especially the case at intermediate to high crystallinities, where segregation of interstitial melt takes place. The differences between this scenario and one more appropriate for non-eutectic magmas, for which the non-linear rate of heat release over time must be considered, is addressed by thermal modelling.

2.3 Thermal modelling

To provide constrains on the timescales of melt extraction, we use thermal modelling to compute the temporal evolution of temperature in instantaneously emplaced cylindrical magma bodies of various volumes, aspect ratios and initial water contents. We solved the two-dimensional axisymmetric formulation of the heat conduction equation, which can be written as:

$$\rho c \frac{\partial T}{\partial t} = \frac{1}{r}\frac{\partial}{\partial r}\left(rk\frac{\partial T}{\partial r}\right) + \frac{\partial}{\partial z}\left(k\frac{\partial T}{\partial z}\right) + \rho L \frac{\partial X_c}{\partial t} \quad (1)$$

were T is the temperature, t is the time, r is the radial coordinate relative to the symmetry axis, z is the depth, k is the thermal conductivity, L is the latent heat of crystallisation, ρ is the density, c is the specific heat and X_c is the fraction of crystals in the magma. For a list of the parameters used in the modelling the reader is referred to Table 2 in the supplementary data. The calculations were performed on a numerical grid using an explicit finite difference discretisation of the above equation. The model considers latent heat of crystallisation, which was implemented using our rhyolite-MELTS results to parametrise the crystal fraction (X_c) versus temperature for the different initial water contents used in this study (Fig. 5a). As the dependence of X_c on T is non-linear, the governing equation was solved using an iterative strategy. In all

models, we integrated an initial geothermal gradient of 25 °C km^{-1} and a temperature-dependent thermal conductivity (k) as described in Whittington et al. (2009) for average crust. The upper (i.e. surface) and lower boundary (i.e. 25-35 km) in the models was set to a fixed temperature determined by the initial geothermal gradient, while zero flux boundary conditions were imposed on the left and right side. Cooling due to circulation of hydrothermal fluids around the magma reservoir was neglected in the modelling and the potential effects of this simplification are discussed in the following.

The setup consists of a 25 x 25 km domain for magma volumes of 100 and 1000 km^3, and a 35 x 35 km domain for intrusion of 10.000 km^3, using 400 x 400 numerical grid for all simulations (supplementary data: Fig. S1). In each model the magma body was intruded instantaneously at 10 km depth at its liquidus temperature and crystallised to near solidus conditions, as determined by the rhyolite-MELTS simulations. To test the effect of reservoir shapes on the solidification history, we ran models with intrusion aspect ratios of 2 and 10 for magma volumes of 100 and 1000 km^3, while model pluton volumes of 10.000 km^3 were only performed with an aspect ratio of 10, due to the large vertical extent of such reservoirs, which makes the application of a single melt fraction-temperature relation unreasonable. Finally, to compare melt segregation velocities to solidification timescales we tracked the temporal propagation of isotherms and melt fraction with depth in the centre of the intrusion.

3 Results

3.1 Thermal, chemical and physical evolution of dacitic magma

Water has an important effect on phase equilibria as it depresses liquidus temperatures and modifies the relationships between temperature, crystallinity, and the physical properties of

magmas over a wide range of chemical compositions (e.g. viscosity and density of the residual melt; Blatter et al., 2013; Caricchi et al., 2007; Giordano et al., 2008; Hess and Dingwell, 1996; Lange, 1994; Melekhova et al., 2013; Müntener and Ulmer, 2018; Ulmer et al., 2018; Whitney, 1988). Crystallisation of magma leads to a non-linear increase of silica and H_2O content in the residual melt (Fig. 4a-d). Once the residual melt becomes water saturated, H_2O_i-undersaturated magmas join the *T*-melt fraction trajectory of initially water-saturated magma (Fig. 4b). The non-linear relationships between melt fraction and temperature, contributes to modulate both the timescales magma spends at different temperatures, and the temporal evolution of the physical properties of the residual melt during progressive magma crystallisation. In crystallising magma reservoirs, magma spends relatively more time at temperatures at which the rate of crystallisation (i.e. rate of latent heat release) is highest (Caricchi and Blundy, 2015; Marsh, 1981). Thus, if the crystallisation rate increases once rheological locking is achieved, magma will spend relatively more time at these temperature conditions (Huber, 2009, Caricchi and Blundy, 2015). The time is even larger considering that the rate of heat release from magma reservoirs drops with cooling and progressive decrease of the thermal gradient between magma and host rocks.

Magmas with lower water contents will achieve rheological locking at higher temperatures with respect to more water-rich magmas, which will, in turn, impact viscosity, density and velocity of residual melt extraction (Fig. 5b, c; Bachman and Bergantz, 2004). Our calculations show that regardless of the initial water content of the magma, residual melt viscosity increases down to melt fractions of 0.5-0.4 because of decreasing temperature and increasing silica content. At lower melt fractions (<0.4) and once volatile saturation is achieved, the viscosity of the residual melt remains relatively constant independent of the initial water content (Fig. 5b). Relatively dry melts ($H_2O_i \leq 2$ wt.%) reach a maximum in viscosity before joining the same trajectory of water-

richer magmas at lower temperatures (Fig. 5b). The contrast in density between the solid phase and residual melt spans a wide range of values near liquidus conditions (for different H_2O_i) but becomes less dependent on H_2O_i for melt fractions <0.6 (Fig. 5c). The ratio of the difference in density between crystals and residual melt and the viscosity of the residual melt, which is directly related to the velocity of melt extraction (Bachman and Bergantz, 2004), generally increases with water content (Figs. 5b, c).

Based on the physical properties of residual melt and magma, the melt extraction velocity is the fastest for H_2O_i-saturated magmas. However, the total time spent by magma at melt fractions <0.6 (i.e. rheologically locked conditions) is inversely proportional to the initial water content (Fig. 5d). To assess the relative importance of the initial water content on the physical properties of magma and the timescales available for melt segregation to occur, we calculate the velocity of melt extraction by hindered settling (Bachmann and Bergantz, 2004) and compaction (McKenzie, 1984) for granodioritic-dacitic magma for melt fraction <0.6. We notice that the formulations used to calculate the velocity of melt extraction are rather simplified, however, such order of magnitude estimates are important to compare the efficiency of residual melt for magmas with different H_2O_i. We do not consider the presence of excess magmatic fluids (i.e. H_2O, CO_2, S) during melt extraction, which can have both positive and detrimental effects on the efficiency of melt extraction (Boudreau, 2016; Caricchi et al., 2018; Parmigiani et al., 2016; Pistone et al., 2015; Sisson and Bacon, 1999).

3.2 Velocities of melt segregation

Hindered settling and compaction-driven segregation describe the relative motion and separation of liquid (i.e. melt) and solid (i.e. crystal) in a two-phase system (i.e. crystallising magma). The

process of particle settling in a monodisperse suspension is described by hindered settling (equation 2). Compaction-driven segregation defines the process of compacting a porous crystalline mush and resulting melt expulsion (equation 3). A detailed evaluation of hindered settling and compaction-driven segregation processes is presented in Bachmann and Bergantz (2004) and Lee et al. (2015).

To obtain velocities for hindered settling (U_{hs}) and compaction-driven segregation (V_{comp}) for crystallising dacitic magma we use the physical properties obtained from rhyolite-MELTS simulations. We calculate segregation velocities following the equations provided by Bachmann and Bergantz (2004; and references therein):

$$\boldsymbol{U_{hs}} = \frac{\mathbf{2}\cdot\boldsymbol{r}^{\mathbf{2}}\cdot\boldsymbol{g}\cdot\boldsymbol{\Delta\varrho}}{\mathbf{9}\cdot\boldsymbol{\mu}} \frac{(\mathbf{1}-\boldsymbol{c})^{\mathbf{2}}}{(\mathbf{1}+\boldsymbol{c}^{\frac{\mathbf{1}}{\mathbf{3}}})[\frac{\mathbf{5}}{\mathbf{3}}\boldsymbol{c}(\mathbf{1}-\boldsymbol{c})]} \quad (2)$$

$$\boldsymbol{V_{comp}} = \frac{\boldsymbol{\kappa}\cdot(\mathbf{1}-\boldsymbol{\phi})\cdot\Delta\boldsymbol{\varrho}\cdot\boldsymbol{g}}{\boldsymbol{\mu}\cdot\boldsymbol{\phi}} \quad (3)$$

Where r is the crystal radius, g is gravitational acceleration (9.81 ms^{-1}), $\Delta\rho$ is the density difference between crystal and melt, μ is the viscosity, c is the crystal fraction, κ is the permeability and ϕ is the porosity. The permeability is calculated from the porosity, crystal radius and permeability coefficient (k) after McKenzie (1984):

$$\boldsymbol{\kappa} = \frac{\boldsymbol{\phi}^{\mathbf{3}}\cdot\boldsymbol{r}^{\mathbf{2}}}{\boldsymbol{K}(\mathbf{1}-\boldsymbol{\phi})^{\mathbf{2}}} \quad (4)$$

We consider that porosity is equal to melt fraction and we use K values between 50 and 200 (Bachmann and Bergantz, 2004; Pistone et al. 2015). Here we assume monodisperse suspensions of melt and crystals. As magmas contains crystals of different sizes, and this tends to reduce the permeability with respect to monodisperse systems (Bachmann and Bergantz, 2004; Rust and

319 Cashman, 2011), the volumetric rates of melt extraction calculated here for each grain size are
320 maximum estimates.

321 To calculate and compare segregation velocities for dacitic magmas with different initial
322 water content, we first assume that no convection occurs and that magmas are rheologically
323 locked at crystallinities >40 wt.%. Based on Equation 2, velocities for hindered settling vary
324 between 3.6 and 0.06 m yr^{-1} for water-saturated magmas and melt fractions decreasing from 0.6
325 to 0.2 (Fig. 6a) using a crystal radius of 3 mm. Velocities for under-saturated magmas are lower
326 (i.e. 1 wt.% H_2O_i; Fig. 6a) and decrease from about 0.22 to 0.02 m yr^{-1} with increasing
327 crystallinity. Segregation velocities for $H_2O_i \geq 3$ wt.% increase in similar fashion as water
328 saturated melts within the rheologically locked interval (Figs. 5a, 6a). Melt segregation of
329 undersaturated magmas with water content <3 wt.% occurs on timescales up to one magnitude
330 slower as they become water saturated at lower temperature and at higher crystallinities resulting
331 in slower melt extraction velocities. The timescales of melt extraction processes strongly depend
332 on the crystal size and vary by more than one order of magnitude when considering crystal radii
333 of 1 to 5 mm (Fig. 6b).

334 We also calculate the velocity of melt extraction considering compaction using a
335 permeability coefficient of 50 and a crystal radius of 3 mm and obtain values between 2.2 m yr^{-1}
336 and 5.0 x 10^{-4} m yr^{-1} for water saturated magma and between 1.4 x 10^{-1} m yr^{-1} and 3.9 x 10^{-4} m
337 yr^{-1} for water undersaturated magma. Segregation velocities decrease up to one order of
338 magnitude when applying larger permeability coefficients (i.e. 100-200; Fig. 6d). Velocities of
339 melt extraction for compaction-driven segregation and hindered settling are similar at melt
340 fractions between 0.6 and 0.5, however, compaction velocities decrease more rapidly with
341 decreasing melt fraction than hindered settling (Bachmann and Bergantz, 2004; Lee et al., 2015).

342 Below melt fractions of 0.2, the velocity of compaction driven segregation has been shown to
343 increase relative to hindered settling (Lee et al., 2015). Our results show that residual melt
344 separates most effectively from highly crystallised dacitic magmas if the initial water
345 concentration is equal or greater than 3 wt.%, independently of the extraction mechanisms
346 considered (Fig. 6). As phase equilibria and H_2O solubility are both affected by pressure, 3 wt.%
347 H_2O_i is a threshold value appropriate for confining pressures of 200 MPa. The increase of H_2O
348 solubility with pressure could increase the efficiency of melt-extraction at mid to deep crustal
349 levels (i.e. 15–20 km depths), where potentially larger H_2O_i would result in lower melt viscosity
350 and accelerate segregation processes. At such depths, the rate of heat release from magma
351 reservoir is also lower, which would also increase the time available for segregation of residual
352 melt.
353
354 *3.3 Crystallisation and melt segregation timescales of hydrous felsic magmas*
355 The thermal modelling results allow us to constrain the crystallisation timescales of hydrous
356 dacitic magmas at melt fraction between 0.6 and 0.2, where segregation is most efficient (Dufek
357 and Bachmann, 2010). We track the position of the isotherm corresponding to a given melt
358 fraction along a vertical section through the middle of the intrusion. Each isotherm propagates
359 from the base and the top of the intrusion toward its inner portions (Fig. 7a). We define the
360 "*maximum segregation timescale*" as the time difference between the moment the isotherms
361 corresponding to melt fractions of 0.6 and 0.2 reach the centre of the intrusion (Fig. 7b).
362 The thermal models show that magmas with low initial water contents (i.e. <3 wt.% H_2O_i) spend
363 substantially more time at rheologically locked conditions than magmas that are initially water-
364 saturated (Fig. 8). For reservoir volumes of 100, 1000, and 10.000 km^3, the maximum timescale

for segregation increase from 13 kyr, 61 kyr and 274 kyr for water saturated magmas to 19 kyr, 84 kyr and 349 kyr, and 20 kyr, 94 kyr and 444 kyr for magmas with initial water contents of 3 and 2 wt.% H_2O_i, respectively. The timescales available for melt segregation increase by a factor of 4 to 5 with decreasing aspect ratios from 10 to 2 (Fig. 8).

To estimate the maximum melt migration distances, we first calculate the average segregation velocity of hindered settling and compaction (Eqs. 2, 3) for each melt fraction interval of 0.1 between 0.6 and 0.2. Secondly, each of these values are multiplied by the time required by the corresponding isotherm to reach the core of the intrusion, once the maximum melt fraction within the reservoir is 0.6 (Figs. 7a and 9a,b). Because of the relatively high segregation velocities at melt fractions between 0.6 and 0.5, the residual melt can migrate large distances over the duration of isotherm propagation from 0.6 to 0.5 (Figs. 6 and 9a,b). For example, maximum segregation distances fall in the order of tens of kilometre for a magma reservoir with a volume of 1000 km^3 (Fig. 9 a,b). The timescales for melt to travel to the roof are fastest for water saturated magma increasing from 600 to 2500 yr for water-saturated magmas and magmas with an initial water content of 2 wt.%, respectively (Fig. 9b). These values decrease to about 300 to 1200 yr for reservoir volumes of 100 km^3 and increase to about 1300 and 5400 years for magma reservoirs with a volume of 10.000 km^3 (Fig. 9b). For a reservoir of 1000 km^3, the time required for the extracted melt to reach the roof by compaction-driven segregation is twice as long and range from 1300 to 5700 yr for water saturated and magma with 2 wt.% H_2O_i, respectively.

4 Discussion

4.1 *Segregation timescales of the Takidani Pluton*

388 Magmas of the Takidani Pluton were initially H_2O-undersaturated with water contents of about 3
389 to 4 wt.% (Hartung et al., 2017; Costa et al., 2004). During crystallisation and melt evolution the
390 residual liquids would have reached volatile saturation at melt fractions between 0.70 (i.e. 4
391 wt.% H_2O_i) and 0.55 (i.e. 3 wt.% H_2O_i) and temperatures around 820°C to 780°C (Fig. 5a,b). At
392 this point an increase of crystallisation rate and release of latent heat of crystallisation would
393 have resulted in near isothermal crystallisation. A potential indication of this process may come
394 from amphibole thermometry, which suggest the crystallisation of this phase occurred almost
395 entirely in between 800 and 750 °C (Hartung et al., 2017). This could supports our hypothesis
396 that magma was thermally buffered over long time periods by the release of latent heat of
397 crystallisation.
398 Based on our rhyolite-MELTS simulations and thermal modelling we estimate the
399 maximum and minimum timescales over which melt segregation took place in the Takidani
400 Pluton. We consider that the column of melt (h) is equal to the thickness of the porphyritic unit
401 (270 m; Fig. 1, Hartung et al. 2017). Velocities of hindered settling segregation of magma with
402 initial water content of 3 to 4 wt.% range from 3.1 m yr^{-1} to about 0.06 m yr^{-1} between 0.6 and
403 0.2 melt fraction for an intermediate crystal radius of 3 mm, which is considered appropriate for
404 granitoids (Bachmann and Bergantz, 2004; Lee et al., 2015) including the Takidani pluton (Fig.
405 1; Hartung et al., 2017). This would imply that the extraction of the melt producing the
406 porphyritic unit of the Takidani pluton required between about 100 yr and 5000 yr. If we
407 considered a smaller crystal size (i.e. 1 mm) the time required for segregation by hindered
408 settling would increase by approximately one order of magnitude to 1000 yr and 45 kyr.
409 Velocities for compaction-driven segregation for the same water contents and crystal size (i.e. 3

410 mm) vary between 0.5 m yr^{-1} and 0.0001 m yr^{-1} leading to much slower extraction timescales of
411 about 800 yr to 2 Myr.
412 The Takidani Pluton has an exposed horizontal extension of about 14 km and exposed
413 vertical extension of about 2 km, which implies a minimum volume of 300 km^3 considering a
414 cylindrical shape. The results of our thermal models show that the time available for segregation
415 in the Takidani Pluton with magmas containing 3 to 4 wt.% H_2O_i varies between 40 and 120 kyr
416 for aspect ratios of 10 and 2, respectively (Fig. 8). The thermal modelling and velocity
417 calculations we performed, show that compaction-driven segregation generally operates at
418 timescales that are larger than estimated solidification timescales and therefore cannot explain
419 the observed segregation in the Takidani Pluton. Hindered settling, on the other side, is a much
420 faster process that can explain the observed melt segregation in the Takidani Pluton. Only in the
421 eventuality that segregation would have started at melt fraction smaller than 0.3, the porphyritic
422 unit of the Takidani pluton would not represent a melt-rich cap near the roof of the pluton.
423 Considering that the base contact of the pluton is tectonic and therefore its volume could be
424 considerably larger than 300 km^3, our results show that sufficient time was available for melt
425 segregation to occur and to form a melt cap via hindered settling (Fig. 10) or processes that
426 operate at similar timescales (i.e. gas filter pressing; Sisson and Bacon, 1999). Moreover,
427 evidence from quartz hosted fluid inclusion studies suggest that the Takidani Pluton developed a
428 liquid-dominated hydrothermal systems at some point in the past (Bando et al., 2003; Sekine et
429 al., 2001). Heat advection associated with hydrothermal circulation is not considered in our
430 calculations but would have increased the rate of heat release depending on the vigour of fluid
431 convection (Delaney et al., 1995). This directly decreases the time available for melt segregation

(Dutrow et al., 2001), thus increasing the potential for melt to form isolated melt lenses instead of large caps on top of magmatic reservoirs.

4.2 The control of H_2O_i on the extraction of residual melt from crystallising magmas

Geochemical and petrologic studies show that crystal poor rhyolites are sourced either from caps at the top of partially crystallised reservoirs (Bachmann and Bergantz, 2004; Hildreth and Wilson, 2007), or from the amalgamation of isolated melt pockets dispersed within a highly crystallised magma (Wotzlaw et al., 2014, Ellis et al., 2014). The processes responsible for the generation of reservoirs with such distinct architecture are not yet fully understood. The total distance over which melt migrates before the system cools to its solidus temperature, controls the final distribution of crystal-poor felsic melt in magmatic reservoirs. Thus, the maximum amount of rhyolitic melt that can potentially be accumulated depends on the initial water content and temperature of the magma, the volume and shape of the magma body and the temperature difference of the intruding magma and the host rock (i.e. thermal gradient). We have illustrated that the initial amount of water dissolved in magmas affects (1) the physical properties and segregation velocities of residual melts (Figs. 5, 6) and (2) the total amount of time spent within the rheologically locked temperature interval (Figs. 7, 8; Caricchi and Blundy, 2015).

Our calculations show that crystal size is an important factor controlling segregation velocities of residual melt (i.e. Bachmann and Bergantz, 2004), while the initial water content affect both the melt extraction velocity and the release of latent heat, which, in turn, modulates the time spent by the magma within different temperature intervals. Volume and shape of the magma reservoir affect the thermal evolution and timescales of reservoir solidification. In case of hindered settling, residual melts of magmas that contain at least 2 wt.% H_2O_i are extracted

455 sufficiently fast to form melt rich caps at or near the roof of the magma reservoir (Fig. 8)
456 considering an intermediate crystal size of 3 mm. Magma reservoirs that have a minimum
457 volume of 1000 km^3 can facilitate complete melt segregation for smaller crystal sizes (Fig.10a).
458 On the other hand, smaller magma bodies (i.e. 100 km^3) with less than 2 wt.% H_2O_i are less
459 likely to form any melt-rich body. Although magmas with 1 wt.% H_2O_i spent half of their
460 solidification time within the rheological locking temperature window (Fig. 5d), the high
461 viscosity of the residual melt (i.e. low segregation velocity) does not favour the formation caps
462 or melt-rich lenses of crystal poor rhyolite under the modelled conditions. The boundaries
463 between caps and lenses, thus, may largely depend on the segregation velocity of the residual
464 melt. Slower segregation of the residual melt, for instance through compaction or through
465 hindered settling in magma with smaller crystals (<3 mm radius; Bachmann and Bergantz,
466 2004), will decrease the probability of forming caps of crystal-poor rhyolitic melt and increase
467 the probability of forming isolated melt-rich lenses.
468 The onset of melt segregation processes can play an important role in the formation of
469 crystal-poor rhyolite (Figs. 9, 10). The likelihood of forming a crystal-poor cap is very high
470 when segregation processes start early within the rheologically locked crystallinity window, and
471 segregation velocities remain elevated (Figs. 6a, 10). Unless magmas are extremely dry (1 wt.%
472 H_2O_i), the initial water content of the magma does not seem to play a major role in controlling
473 the architecture of the reservoir and melt distribution when melt extraction occurs at high melt
474 fractions (i.e. 0.6; Fig. 9a,b). The timescales of melt accumulation, however, are strongly
475 dependent on the type of segregation process (i.e. hindered settling and compaction) and on the
476 initial water content: melts containing higher amounts of water migrate faster (Fig. 9a,b) because
477 of their lower viscosities (Fig. 5b). When the onset of melt segregation occurs at relatively low

478 melt fractions (i.e. 0.3), the initial water content may influence whether caps or separate lenses
479 are formed. Water undersaturated magmas may have a higher chance to form melt caps
480 compared to magmas with higher water contents, because of their prolonged cooling timescales
481 at rheologically locked conditions (Fig.10c). Overall though, at low melt fraction timescales for
482 melt segregation are short, which together with low melt migration velocities decreases the
483 capacity of these magmas to form thick melt rich bodies near the roof of the reservoir and the
484 formation of isolated melt rich lenses becomes more likely.
485
486 **5 Conclusions**
487 The interplay between magma water content, the viscosity of residual melt, the density contrast
488 between residual melt and crystals, and the time spent within the rheologically locked
489 crystallinity interval, favoured the extraction of residual melt from the Takidani pluton (Fig. 5).
490 Our time estimates for melt segregation indicate that the extraction of residual liquids in silicic
491 reservoirs like the Takidani Pluton occurs over centuries and millennia which is consistent with
492 other studies (Bachmann and Huber, 2018).
493 While the initial water content in magma has a significant control on the segregation
494 timescales of magmatic reservoirs, the architecture of magmatic reservoirs is controlled by the
495 magma crystallinity, crystal size and permeability at the onset of melt segregation processes. The
496 results from our models suggest that hydrous felsic magma are prone to form large melt caps at
497 the roof of a magma reservoir if segregation occurs early at intermediate melt fractions (e.g. 0.6-
498 0.5). However, if segregation starts at low melt fractions (i.e. compaction-driven segregation),
499 silica-rich melts may not be able to reach the roof of magma reservoirs because of their low
500 segregation velocity and may form isolated melt lenses within highly crystallised magma. A

similar reservoir configuration is likely for water-poor magmas, as residual melt segregation require longer timescales (Fig. 7). The drainage of isolated crystal poor lenses of magma during eruption may account for the chemically heterogeneous nature of rhyolitic eruptions in relatively dry systems such as Yellowstone (Ellis et al., 2014; Wotzlaw et al., 2014). We notice that our study focuses on felsic magmas characteristic of some of the large eruptions on Earth; the dependency of viscosity and density of magma and residual melt on chemistry does not warrant the extension of our conclusions to systems of significantly different chemistry.

The timescales of melt segregation vary by several orders depending on the crystal size and the mechanism that dominates the extraction process (Fig. 6b). The extremely short timescales obtained from geochronology and geospeedometry (months to decades; Druitt et al., 2012; Gualda et al., 2018; Wilson and Charlier, 2016), are difficult to explain by gravity-driven segregation even considering a large crystal size (>5 mm).

Despite limitations, our calculations provide a framework to deduce some of the additional factors that may influence the capacity of magmatic systems to contain lenses or caps of eruptible felsic melt. For example, large systems such as Yellowstone host well-developed hydrothermal systems, which increases the rate of heat extraction from magmatic systems with respect to what we consider here. This directly decreases the time available for melt segregation (Dutrow et al., 2001), thus increasing the potential for melt to form isolated melt lenses instead of large caps on top of magmatic reservoirs. Ultimately the complex feedbacks between magma chemistry and its physical properties and the thermal evolution of magmatic systems require a multidisciplinary approach (Gualda et al., 2018; Holness, 2018; Huber and Parmigiani, 2018) to identify the potential signs of an impending volcanic eruption. Our results suggest that for hydrous felsic magmatic systems the initial water content of magma play an important role on

the extraction of residual by affecting both the evolution of the physical properties of magma with temperature and the time magma spends within different temperature intervals.

6 Acknowledgements

We are grateful to Guilherme Gualda and an anonymous reviewer for their detailed and constructive feedback, which has significantly improved this article. We would also like to thank the editor Tamsin Mather for handling this contribution and additional insightful comments. This project was supported by the Swiss National Science Foundation [SNSF grant 200021_150204]. EH was also financially supported by the Japan Society for the Promotion of Science (GR17103). LC and GW received additional funding from the European Research Council (ERC) under the European Union's Horizon 2020 research and innovation program (grant agreement 677493-FEVER).

7 References

Andersen, N.L., Singer, B.S., Jicha, B.R., Beard, B.L., Johnson, C.M., Licciardi, J.M., 2017. Pleistocene to holocene growth of a large upper crustal rhyolitic magma reservoir beneath the active laguna del Maule Volcanic Field, Central Chile. J. Petrol. 58, 85–114. https://doi.org/10.1093/petrology/egx006

Bachmann, O., Bergantz, G., 2004. On the Origin of Crystal-poor Rhyolites : Extracted from Batholithic Crystal Mushes. J. Petrol. 45, 1565–1582. https://doi.org/10.1093/petrology/egh019

Bachmann, O., Huber, C., 2018. The inner workings of crustal distillation columns; the physical mechanisms and rates controlling phase separation in silicic magma reservoirs. J. Petrol.

egy103. https://doi.org/10.1093/petrology/egy103

Bando, M., Bignall, G., Sekine, K., Tsuchiya, N., 2003. Petrography and uplift history of the Quaternary Takidani Granodiorite : could it have hosted a supercritical (HDR) geothermal reservoir? J. Volcanol. Geotherm. Res. 120, 215–234.

Barnes, C.G., Berry, R., Barnes, M.A., Ernst, W.G., 2017. Trace element zoning in hornblende: Tracking and modeling the crystallization of a calc-alkaline arc pluton. Am. Mineral. 102, 2390–2405. https://doi.org/10.2138/am-2017-6063

Bedrosian, P.A., Peacock, J.R., Bowles-Martinez, E., Schultz, A., Hill, G.J., 2018. Crustal inheritance and a top-down control on arc magmatism at Mount St Helens. Nat. Geosci. 11, 865–870. https://doi.org/10.1038/s41561-018-0217-2

Blatter, D.L., Sisson, T.W., Hankins, W. Ben, 2013. Crystallization of oxidized, moderately hydrous arc basalt at mid- to lower-crustal pressures: Implications for andesite genesis. Contrib. to Mineral. Petrol. 166, 861–886. https://doi.org/10.1007/s00410-013-0920-3

Bottinga, Y., Weill, D.F., 1972. The viscosity of magmatic silicate liquids; a model calculation. Am. J. Sci. 272, 438–475. https://doi.org/10.2475/ajs.272.5.438

Boudreau, A., 2016. Bubble migration in a compacting crystal-liquid mush. Contrib. to Mineral. Petrol. 171, 32. https://doi.org/10.1007/s00410-016-1237-9

Caricchi, L., Blundy, J., 2015. Experimental petrology of monotonous intermediate magmas. Geol. Soc. London, Spec. Publ. 422, 105–130. https://doi.org/10.1144/SP422.9

Caricchi, L., Burlini, L., Ulmer, P., Gerya, T., Vassalli, M., Papale, P., 2007. Non-Newtonian rheology of crystal-bearing magmas and implications for magma ascent dynamics. Earth Planet. Sci. Lett. 264, 402–419. https://doi.org/10.1016/j.epsl.2007.09.032

Caricchi, L., Sheldrake, T.E., Blundy, J., 2018. Modulation of magmatic processes by

CO2flushing. Earth Planet. Sci. Lett. 491, 160–171. https://doi.org/10.1016/j.epsl.2018.03.042

Coleman, D.S., Gray, W., Glazner, A.F., 2004. Rethinking the emplacement and evolution of zoned plutons: Geochronologic evidence for incremental assembly of the Tuolumne Intrusive Suite, California. Geology 32, 433–436. https://doi.org/10.1130/G20220.1

Costa, F., Scaillet, B., Pichavant, M., 2004. Petrological and Experimental Constraints on the Pre-eruption Conditions of Holocene Dacite from Volcan San Pedro (36°S, Chilean Andes) and the Importance of Sulphur in Silicic Subduction-related Magmas. J. Petrol. 45, 855–881. https://doi.org/10.1093/petrology/egg114

Davis, R.H., Acrivos, A., 1985. Sedimentation of Noncolloidal Particles at Low Reynolds Numbers. Annu. Rev. Fluid Mech. 17, 91–118. https://doi.org/10.1146/annurev.fl.17.010185.000515

Deering, C.D., Cole, J.W., Vogel, T.A., 2011. Extraction of crystal-poor rhyolite from a hornblende-bearing intermediate mush: A case study of the caldera-forming Matahina eruption, Okataina volcanic complex. Contrib. to Mineral. Petrol. 161. https://doi.org/10.1007/s00410-010-0524-0

Delaney, P.T., Sass, J.H., Duffield, W.A., Kauahikaua, J.P., 1995. Temperature and response time of magma hydrothermal systems, with an example from Kilauea, Hawaii. [Proceedings] 1239–1244.

Druitt, T.H., Costa, F., Deloule, E., Dungan, M., Scaillet, B., 2012. Decadal to monthly timescales of magma transfer and reservoir growth at a caldera volcano. Nature 482, 77–80. https://doi.org/10.1038/nature10706

Dufek, J., Bachmann, O., 2010. Quantum magmatism: Magmatic compositional gaps generated

by melt-crystal dynamics. Geology 38, 687–690. https://doi.org/10.1130/G30831.1

Dutrow, B.L., Travis, B.J., Gable, C.W., Henry, D.J., 2001. Coupled heat and silica transport associated with dike intrusion into sedimentary rock: effects on isotherm location and permeability evolution. Geochim. Cosmochim. Acta 65, 3749–3767. https://doi.org/https://doi.org/10.1016/S0016-7037(01)00704-9

Ellis, B.S., Bachmann, O., Wolff, J. a., 2014. Cumulate fragments in silicic ignimbrites: The case of the Snake River Plain. Geology 42, 431–434. https://doi.org/10.1130/G35399.1

Gelman, S.E., Deering, C.D., Bachmann, O., Huber, C., Gutiérrez, F.J., 2014. Identifying the crystal graveyards remaining after large silicic eruptions. Earth Planet. Sci. Lett. 403, 299–306. https://doi.org/10.1016/j.epsl.2014.07.005

Giordano, D., Russell, J.K., Dingwell, D.B., 2008. Viscosity of magmatic liquids: A model. Earth Planet. Sci. Lett. 271, 123–134. https://doi.org/10.1016/j.epsl.2008.03.038

Gualda, G.A.R., Ghiorso, M.S., Lemons, R. V., Carley, T.L., 2012. Rhyolite-MELTS: a Modified Calibration of MELTS Optimized for Silica-rich, Fluid-bearing Magmatic Systems. J. Petrol. 53, 875–890. https://doi.org/10.1093/petrology/egr080

Gualda, G.A.R., Gravley, D.M., Conner, M., Hollmann, B., Pamukcu, A.S., Bégué, F., Ghiorso, M.S., Deering, C.D., 2018. Climbing the crustal ladder: Magma storage-depth evolution during a volcanic flare-up. Nat. Commun. 1–10. https://doi.org/10.1093/gji/ggw416

Harayama, S., 1994. Cooling History of the youngest exposed pluton in the World - The Plio-Pleistocene Takidani Granodiorite (Japan Alps, central Japan). Mem. Geol. Soc. Japan 43, 87–97.

Harayama, S., 1992. Geology Youngest exposed granitoid pluton on Earth : Cooling and rapid uplift of the Pliocene-Quaternary Takidani Granidiorite in the Japan Alps, central Japan.

Geology 20, 657–660. https://doi.org/10.1130/0091-7613(1992)020<0657

Harayama, S., Wada, H., Yamaguchi, Y., 2003. Trip A1 Quaternary and Pliocene granites in the Northern Japan Alps. Hutt. Symp. V, F. Guideb.

Hartung, E., Caricchi, L., Floess, D., Wallis, S., Harayama, S., Kouzmanov, K., Chiaradia, M., 2017. Evidence for residual melt extraction in the Takidani Pluton, Central Japan. J. Petrol. 58, 763–788. https://doi.org/10.1093/petrology/egx033

Hess, K.U., Dingwell, D.B., 1996. Viscosities of hydrous leucogranitic melts : A non-Arrhenian on the nature and efficiency of magmatic processes . As pendence (H20 concentration in weight percent) for each. Am. Mineral. 81, 1297–1300. https://doi.org/10.1016/0016-7037(82)90381-7

Hildreth, W., 2004. Volcanological perspectives on Long Valley , Mammoth Mountain , and Mono Craters : several contiguous but discrete systems. J. Volcanol. Geotherm. Res. 136, 169–198. https://doi.org/10.1016/j.jvolgeores.2004.05.019

Hildreth, W., 1981. Gradients in silicic magma chambers: Implications for lithospheric magmatism. J. Geophys. Res. Solid Earth 86, 10153–10192. https://doi.org/10.1029/JB086iB11p10153

Hildreth, W., Wilson, C.J.N., 2007. Compositional Zoning of the Bishop Tuff. J. Petrol. 48, 951–999. https://doi.org/10.1093/petrology/egm007

Holness, M.B., 2018. Melt segregation from silicic crystal mushes: a critical appraisal of possible mechanisms and their microstructural record. Contrib. to Mineral. Petrol. 173, 1–17. https://doi.org/10.1007/s00410-018-1465-2

Holness, M.B., Vukmanovic, Z., Mariani, E., 2017. Assessing the role of compaction in the formation of adcumulates: A microstructural perspective. J. Petrol. 58, 643–674.

https://doi.org/10.1093/petrology/egx037

Holtz, F., Sato, H., Lewis, J., Behrens, H., Nakada, S., 2005. Experimental petrology of the 1991-1995 Unzen dacite, Japan. Part I: Phase relations, phase composition and pre-eruptive conditions. J. Petrol. 46, 319–337. https://doi.org/10.1093/petrology/egh077

Huang, H.-H., Lin, F.-C., Schmandt, B., Farrell, J., Smith, R.B., Tsai, V.C., 2015. The Yellowstone magmatic system from the mantle plume to the upper crust. Science (80-.). 348, 773 LP-776.

Huber, C., Bachmann, O., Dufek, J., 2012. Crystal-poor versus crystal-rich ignimbrites : A competition between stirring and reactivation. Society 1–4. https://doi.org/10.1130/G32425.1

Huber, C., Bachmann, O., Dufek, J., 2010. The limitations of melting on the reactivation of silicic mushes. J. Volcanol. Geotherm. Res. 195, 97–105. https://doi.org/10.1016/j.jvolgeores.2010.06.006

Huber, C., Bachmann, O., Manga, M., 2009. Homogenization processes in silicic magma chambers by stirring and mushification (latent heat buffering). Earth Planet. Sci. Lett. 283, 38–47. https://doi.org/10.1016/j.epsl.2009.03.029

Huber, C., Parmigiani, A., 2018. A Physical Model for Three-Phase Compaction in Silicic Magma Reservoirs. J. Geophys. Res. Solid Earth 2685–2705. https://doi.org/10.1002/2017JB015224

Ito, H., Spencer, C.J., Danišík, M., Hoiland, C.W., 2017. Magmatic tempo of Earth's youngest exposed plutons as revealed by detrital zircon U-Pb geochronology. Sci. Rep. 7, 12457. https://doi.org/10.1038/s41598-017-12790-w

Johannes, W., Holtz, F., 1996. Petrogenesis and Experimental Petrology of Granitic Rocks.

662 Springer-Verlag, Berlin, Heidelberg, New York.
663 Kimura, J.-I., Nagahashi, Y., 2007. Origin of a voluminous iron-enriched high-K rhyolite magma
664 erupted in the North Japan Alps at 1.75 Ma: Evidence for upper crustal melting. J.
665 Volcanol. Geotherm. Res. 167, 81–99. https://doi.org/10.1016/j.jvolgeores.2007.02.004
666 Lange, R.A., 1994. The Effects of H2O, CO2 and F on the Density and Viscosity of Silicate
667 Melts. Rev. Mineral. Geochemistry 30, 331–370.
668 Lee, C.-T.A., Morton, D.M., Farner, M.J., Moitra, P., 2015. Field and model constraints on
669 silicic melt segregation by compaction/hindered settling: The role of water and its effect on
670 latent heat release. Am. Mineral. 100, 1762–1777.
671 Marsh, B.D., 1981. On the crystallinity, probability of occurrence, and rheology of lava and
672 magma. Contrib. to Mineral. Petrol. 78, 85–98. https://doi.org/10.1007/BF00371146
673 McKenzie, D., 1984. The generation and compactation of partially molten rock. J. Petrol. 25,
674 713–765.
675 Melekhova, E., Annen, C., Blundy, J., 2013. Compositional gaps in igneous rock suites
676 controlled by magma system heat and water content. Nat. Geosci. 6, 385–390.
677 https://doi.org/10.1038/ngeo1781
678 Müntener, O., Ulmer, P., 2018. Arc crust formation and differentiation constrained by
679 experimental petrology. Am. J. Sci. https://doi.org/10.2475/01.2018.04
680 Nagahashi, Y., Satoguchi, Y., Yoshikawa, S., 2000. Correlation and stratigraphic eruption age of
681 the pyroclastic flow deposits and wide spread volcanic ashes intercalated in the Pliocene-
682 Pleistocene strata, central Japan. J. Geol. Soc. Japan 106, 51–69.
683 Parmigiani, A., Faroughi, S., Huber, C., Bachmann, O., Su, Y., 2016. Bubble accumulation and
684 its role in the evolution of magma reservoirs in the upper crust. Nature 532, 492–495.

https://doi.org/10.1038/nature17401

Pistone, M., Arzilli, F., Dobson, K.J., Cordonnier, B., Reusser, E., Ulmer, P., Marone, F., Whittington, A.G., Mancini, L., Fife, J.L., Blundy, J.D., 2015. Gas-driven filter pressing in magmas: Insights into in-situ melt segregation from crystal mushes. Geology 43, G36766.1. https://doi.org/10.1130/G36766.1

Rudnick, R.L., Gao, S., 2003. Composition of the Continental Crust, in: Treatise on Geochemistry. Elsevier, pp. 1–64. https://doi.org/10.1016/B0-08-043751-6/03016-4

Rust, A.C., Cashman, K. V., 2011. Permeability controls on expansion and size distributions of pyroclasts. J. Geophys. Res. Solid Earth 116, 1–17. https://doi.org/10.1029/2011JB008494

Scaillet, B., Evans, B.W., 1999. The 15 June 1991 Eruption of Mount Pinatubo . I . Phase Equilibria and Pre-eruption P–T–fO2–fH2O Conditions of the Dacite Magma. J. Petrol. 40, 381–411.

Sekine, K., Bignall, G., Tsuchiya, N., Nakatsuka, K., 2001. Evidence for Fluid Flow in Non-Brittle Takidani Granite Implications for Utilization of DSGRs. Geotherm. Resour. Counc. Trans. 25, 243–248.

Sisson, T.W., Bacon, C.R., 1999. Gas-driven filter pressing in magmas. Geology 27, 613–616. https://doi.org/10.1130/0091-7613(1999)027<0613

Ulmer, P., Kaegi, R., Müntener, O., 2018. Experimentally derived intermediate to silica-rich arc magmas by fractional and equilibrium crystallization at 1·0 GPa: An evaluation of phase relationships, compositions, liquid lines of descent and oxygen fugacity. J. Petrol. 59, 11–58. https://doi.org/10.1093/petrology/egy017

Vigneresse, J.-L., 2014. Textures and melt-crystal-gas interactions in granites. Geosci. Front. https://doi.org/10.1016/j.gsf.2014.12.004

Whitney, J.A., 1988. The origin of granite: The role and source of water in the evolution of granitic magmas. Geol. Soc. Am. Bull. 100, 1886–1897.

Whittington, A.G., Hofmeister, A.M., Nabelek, P.I., 2009. Temperature-dependent thermal diffusivity of the Earth's crust and implications for magmatism. Nature 458, 319–21. https://doi.org/10.1038/nature07818

Wilson, C.J.N., Charlier, B.L.A., 2016. The life and times of silicic volcanic systems. Elements 12, 103–108. https://doi.org/10.2113/gselements.12.2.103

Wotzlaw, J.-F., Bindeman, I.N., Watts, K.E., Schmitt, A.K., Caricchi, L., Schaltegger, U., 2014. Linking rapid magma reservoir assembly and eruption trigger mechanisms at evolved Yellowstone-type supervolcanoes. Geology 42, 807–810. https://doi.org/10.1130/G35979.1

720 FIGURE CAPTIONS

721

722 Figure 1:

723 Evidence for melt segregation in the upper section of the Takidani Pluton. (left) QEMSCAN
724 images collected from the granodiorite (1; GDT) to the porphyritic portion of the pluton (5;
725 pGT). (top right) Variations of Rb and Sr whole-rock content from GDT to pGT. (bottom right)
726 Interstitial residual melt variations represented by quartz (pink), orthoclase (green) and
727 plagioclase with anorthite content <30 wt.% (orange). The fraction of interstitial residual melt
728 (x_{melt}), gradually increases from the GDT unit towards the pGT unit. The content of quartz,
729 orthoclase and albite, normalised to a fraction of 1, remain relative constant and suggest that the
730 residual melt composition was buffered at the granitic minimum (Johannes and Holtz, 1996).

731

732 Figure 2:

733 Chemical variability in whole rock (a) and mineral chemistry (b). (a) Assimilation and fractional
734 crystallisation (AFC) models (Hartung et al., 2017) performed on whole rock analyses show that
735 compositional diversity is dominantly produced by crystal fractionation. The grey dashed lines
736 and numbers on the side show the amount of melt (i.e. 60 wt.%) and assimilation (i.e. 3.2 wt.%).
737 The evolution of Rb concentration as function of $^{86}Sr/^{87}Sr$ is calculated for different bulk
738 partition coefficients (D_{Rb}). (b) Concentrations of Rb in plagioclase phenocrysts (i.e. sample
739 EH70) increase from 0.54 to 1.31 ppm from core to rim, respectively, and point towards a
740 progressive enrichment of the incompatible element Rb in the melt phase through crystal
741 fractionation. The grey dashed lines and number below indicate the amount of melt fraction.

742

743 Figure 3:

744 Comparison between rhyolite-MELTS simulations (lines) and the matrix glass compositions
745 (circles) measured between 950°C and 800°C by Costa et al. (2004). The colour contouring
746 indicates the initial water content of the starting material (Costa et al. 2004). Rhyolite-MELTS
747 and experiments are in broad agreement and show the effect of initial water content on the
748 chemical evolution (i.e. SiO_2, Al_2O_3, Na_2O, K_2O) of residual melt with decreasing temperature.
749 No experimental data is available below 800°C.

750

751 Figure 4:

752 Results of rhyolite-MELTS simulations for dacitic magma with composition similar to the
753 Takidani granodiorite and the starting material of Costa et al. (2004). (a) Evolution of the water
754 content of the residual melt as function of temperature. (b) Relationship between water content
755 of the residual melt and melt fraction. (c) Silica content of the residual melt versus temperature.
756 (d) Water content versus silica content of the residual melt.

757

758 Figure 5:

759 Physical melt fraction and physical properties of residual melt and magma calculated with
760 rhyolite-MELTS. (a) Relationship between melt fraction and temperature. (b) Evolution of melt
761 viscosity (logarithmic) as function of melt fraction. (c) Density difference between crystals and
762 the residual melt as function of melt fraction. (d) Fraction of the total time spent by the magma
763 within each interval of melt fraction. This is calculated by normalising the number of simulation
764 step within a melt fraction unit of 0.02 to the total amount of steps between 1.0 and 0.1 melt
765 fraction assuming constant heat loss.

Figure 6:

Velocities of melt segregation as function of the melt fraction for magma with different water content for hindered settling (a, b) and compaction-driven segregation (c, d). (a) Hindered settling velocity for different initial water contents (H_2O_i) and crystal radius of 3 mm. (b) Hindered settling velocity for water saturated magma containing crystals of different radii (r). (c) Velocity of compaction-driven segregation for different initial water content and magma with crystal of 3 mm radius. (d) Compaction-driven segregation velocity for water-saturated magma, calculated for different permeability coefficients (K) and crystal radius of 3 mm. Segregation velocities are calculated using the physical properties obtained from rhyolite-MELTS simulations.

Figure 7:

(a) Vertical position of the isotherms, corresponding to different melt fractions (Mf), along a vertical section through the centre of the intrusion as function of time. Reservoir thickness of 0 m presents the top. Location of isotherms are shown for a dacitic magma with initial water content of 2 wt.%. (b) Maximum segregation timescales for magma reservoirs with different initial water content. Isotherm curves are shown for a magma reservoir of 1000 km^3 with an aspect ratio (AR) of 10. The Maximum segregation timescale increases with decreasing initial water content of the magma.

Figure 8:

Maximum timescales available for segregation for different reservoir volumes, water contents and aspect ratios of the magma reservoir. Curves were obtained by fitting the thermal modelling results using 2nd and 3rd order polynomials (supplementary data: Table 3).

Figure 9:

(a, b) Maximum segregation distance for a reservoir volume of 1000 km^3 and aspect ratio of 10 based on hindered settling and compaction velocities corresponding to an intermediate crystal radius (i.e. r = 3 mm). (c, d) Time required by the residual melt (extracted by hindered settling and compaction) to reach the roof of the magma reservoir for reservoirs of 100, 1000 and 10.000 km^3. The y axis presents the onset on melt segregation for intervals of 0.1 starting at 0.6, 0.5, 0.4 and 0.3.

Figure 10:

Schematic model for the formation of melt caps and melt pockets for different volumes and water contents for hindered settling. (a) Full segregation is expected in reservoir >100 km^3 for crystal radii >1 mm for the case that segregation processes start at melt fraction of 0.5 or higher. (b) When melt segregation starts at Mf<0.4 only reservoirs that are larger than 100 km^3 or that have low initial water contents are expected to form melt caps. (c) Partial melt segregation and the formation of crystal lenses are most likely to occur if segregation occurs at high crystallinity. Solidification of the reservoir without significant segregation is expected for magmas with water contents <<2 wt.%. The Takidani Pluton most likely formed a coherent melt cap that may have been erupted.

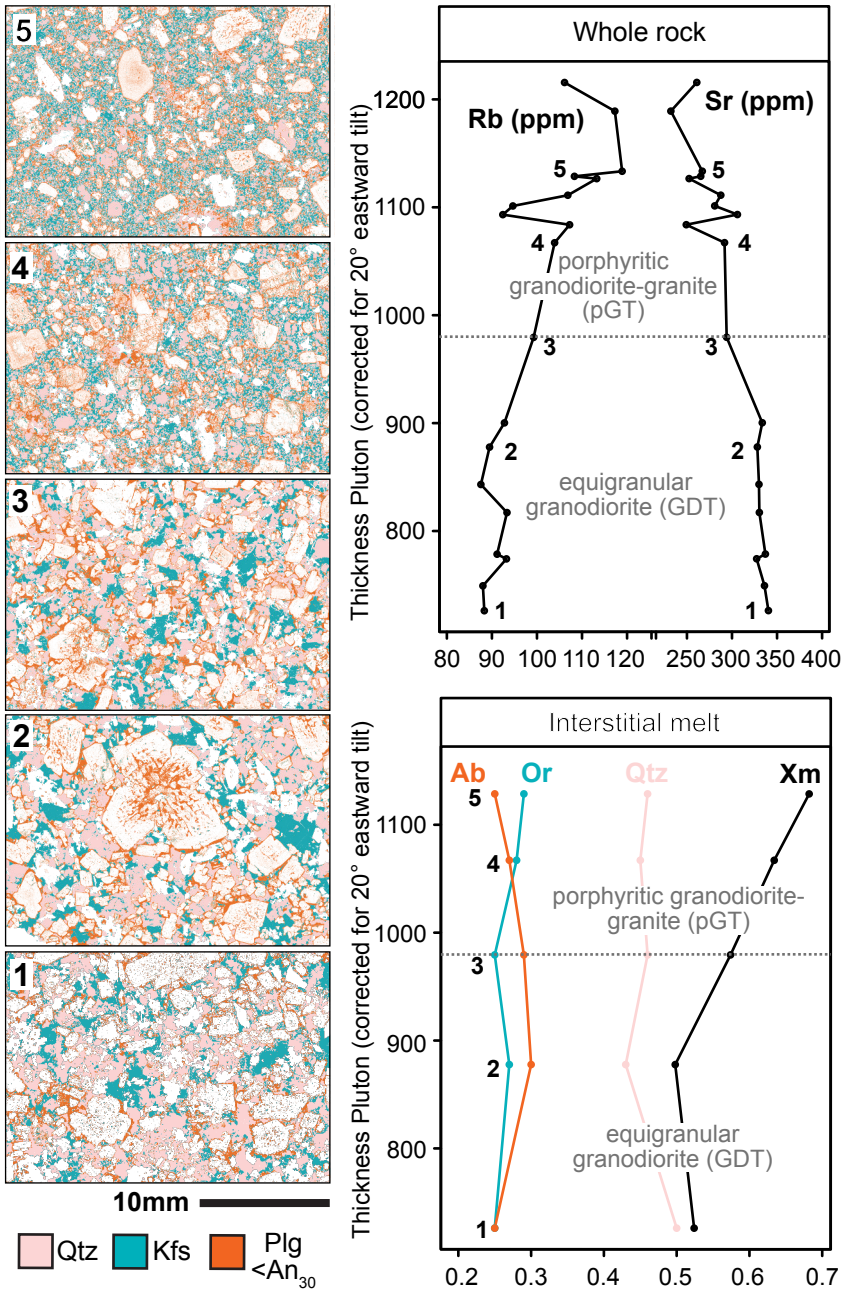
5
4
3
2
1
10mm
Qtz
Kfs
Plg
<An30
Whole rock
Rb (ppm)
Sr (ppm)
porphyritic
granodiorite-granite
(pGT)
equigranular
granodiorite (GDT)
Thickness Pluton (corrected for 20° eastward tilt)
1200
1100
1000
900
800
80 90 100 110 120
250 300 350 400
Interstitial melt
Ab
Or
Qtz
Xm
porphyritic granodiorite-
granite (pGT)
equigranular
granodiorite (GDT)
0.2 0.3 0.4 0.5 0.6 0.7

810

811

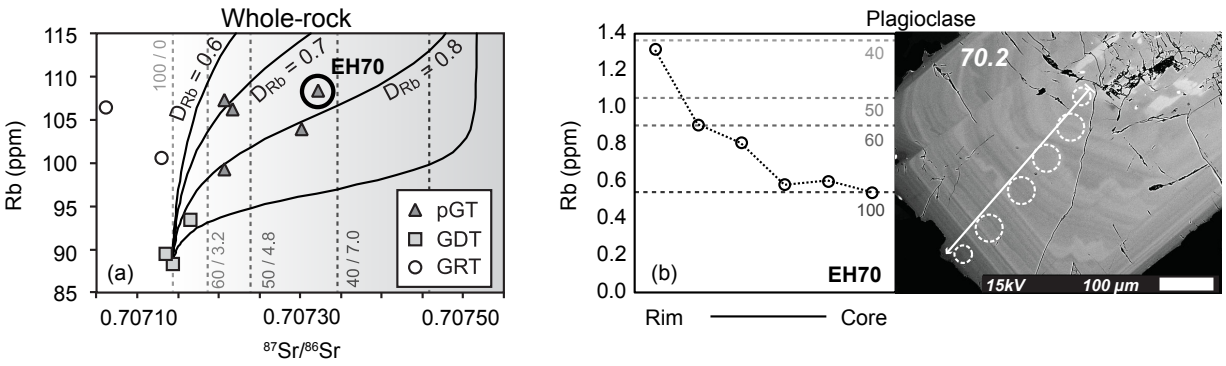
Whole-rock
Rb (ppm)
115
110
105
100
95
90
85
0.70710
0.70730
0.70750
87Sr/86Sr
100 / 0
DRb = 0.6
DRb = 0.7
DRb = 0.8
EH70
60 / 3.2
50 / 4.8
40 / 7.0
pGT
GDT
GRT
(a)
Plagioclase
Rb (ppm)
1.4
1.2
1.0
0.8
0.6
0.4
0.2
0.0
40
50
60
100
70.2
(b)
EH70
15kV
100 µm
Rim
Core

812

813

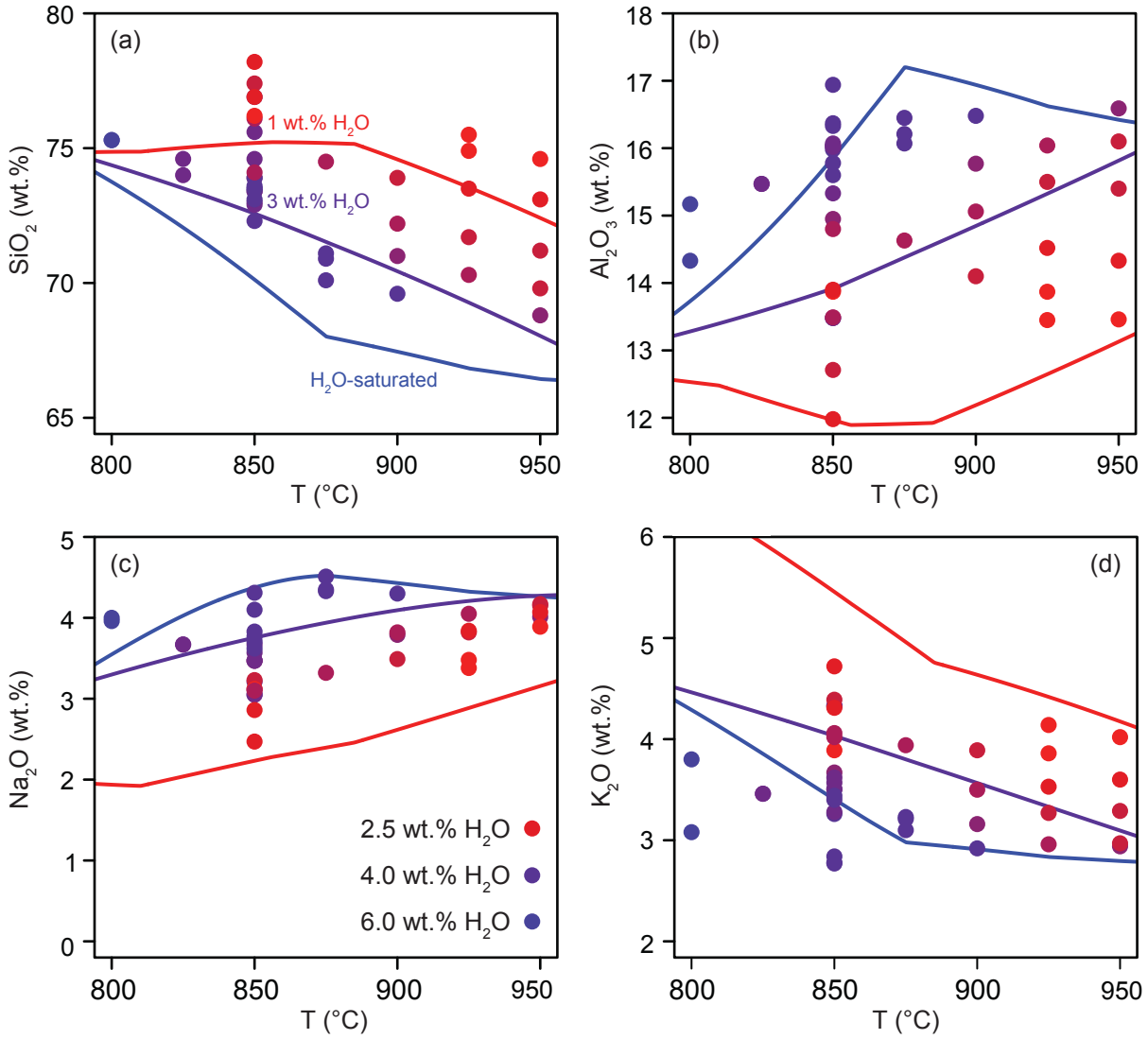
(a)
1 wt.% H2O
3 wt.% H2O
H2O-saturated
SiO2 (wt.%)
T (°C)
(b)
Al2O3 (wt.%)
T (°C)
(c)
Na2O (wt.%)
2.5 wt.% H2O
4.0 wt.% H2O
6.0 wt.% H2O
T (°C)
(d)
K2O (wt.%)
T (°C)

814

815

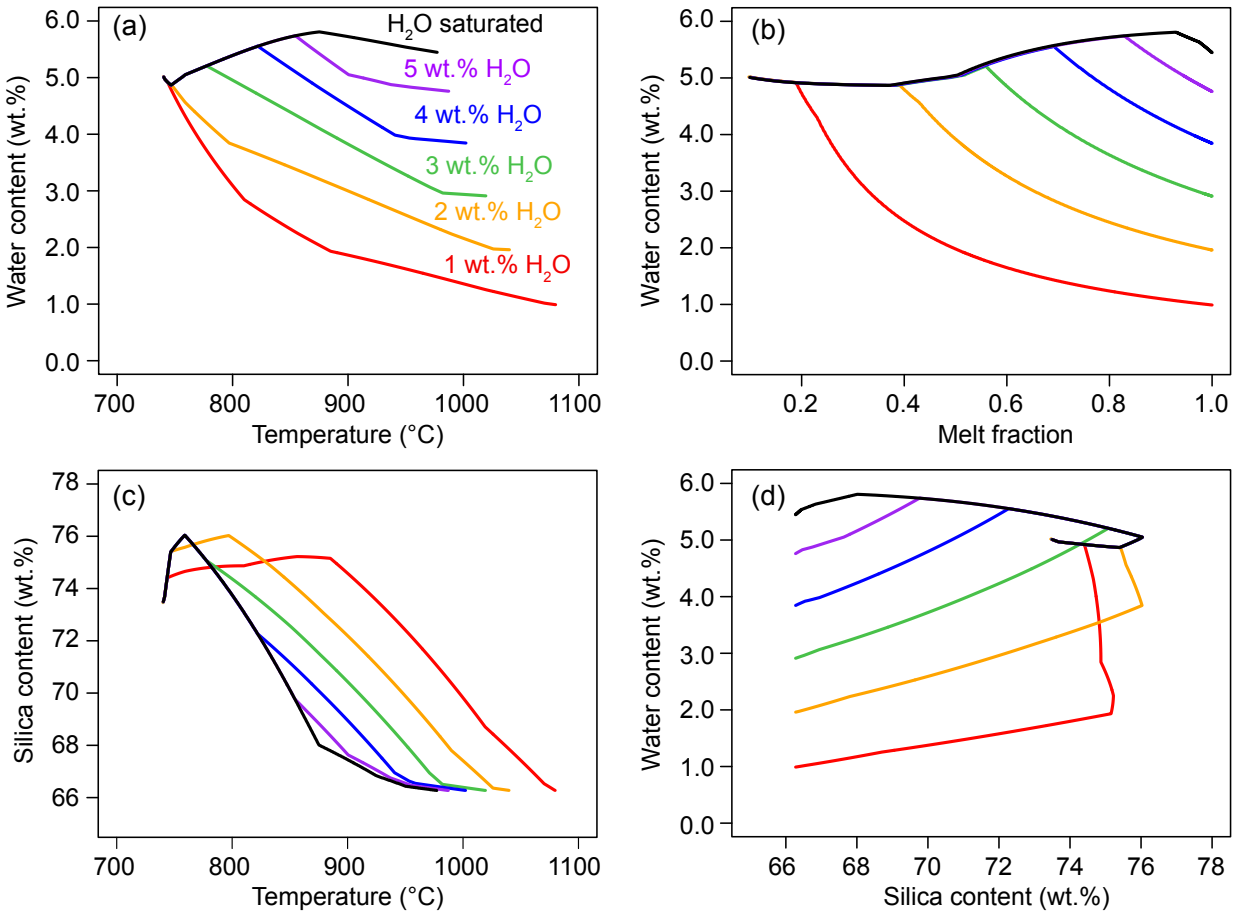
(a)
H2O saturated
5 wt.% H2O
4 wt.% H2O
3 wt.% H2O
2 wt.% H2O
1 wt.% H2O
Water content (wt.%)
Temperature (°C)
(b)
Water content (wt.%)
Melt fraction
(c)
Silica content (wt.%)
Temperature (°C)
(d)
Water content (wt.%)
Silica content (wt.%)

816

817

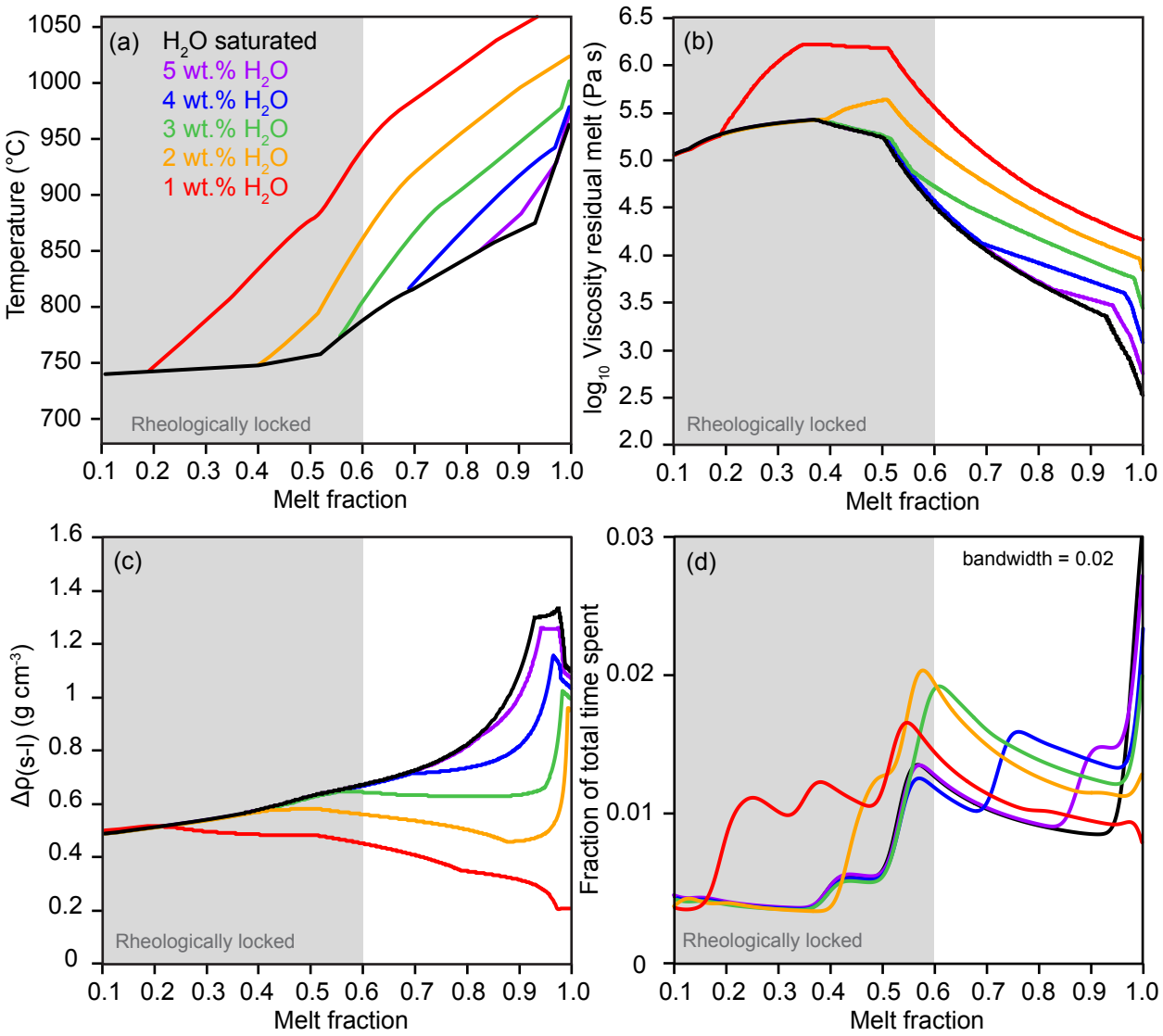
(a)
H2O saturated
5 wt.% H2O
4 wt.% H2O
3 wt.% H2O
2 wt.% H2O
1 wt.% H2O
Temperature (°C)
Melt fraction
Rheologically locked
(b)
log10 Viscosity residual melt (Pa s)
Melt fraction
Rheologically locked
(c)
Δρ(s-l) (g cm-3)
Melt fraction
Rheologically locked
(d)
bandwidth = 0.02
Fraction of total time spent
Melt fraction
Rheologically locked

818

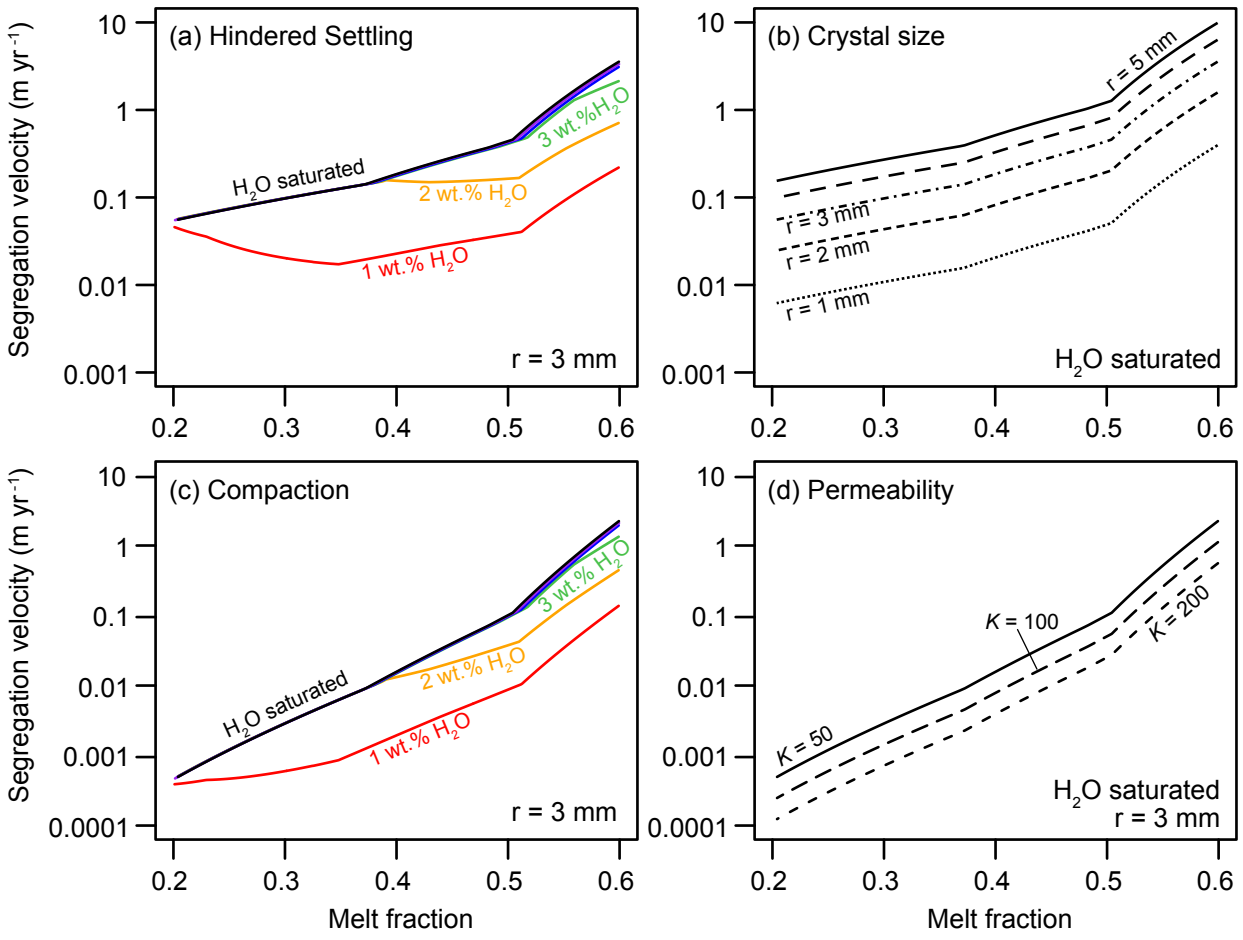
(a) Hindered Settling
H2O saturated
3 wt.%H2O
2 wt.% H2O
1 wt.% H2O
r = 3 mm
(b) Crystal size
r = 5 mm
r = 3 mm
r = 2 mm
r = 1 mm
H2O saturated
(c) Compaction
H2O saturated
3 wt.% H2O
2 wt.% H2O
1 wt.% H2O
r = 3 mm
(d) Permeability
K = 100
K = 200
K = 50
H2O saturated
r = 3 mm
Segregation velocity (m yr-1)
Melt fraction

819

820

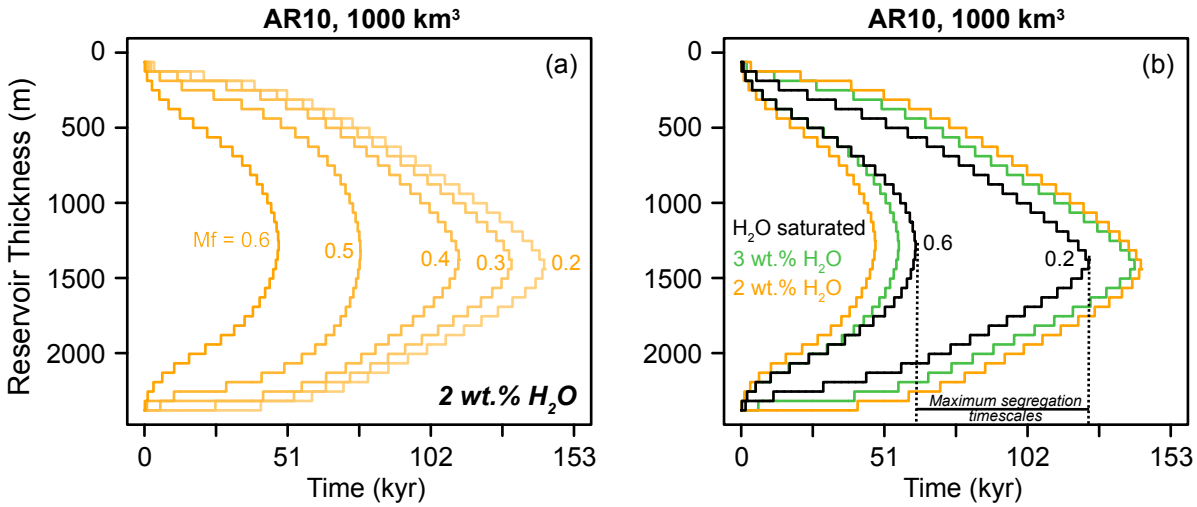
AR10, 1000 km³
(a)
Reservoir Thickness (m)
0
500
1000
1500
2000
Mf = 0.6
0.5
0.4
0.3
0.2
2 wt.% H2O
0
51
102
153
Time (kyr)
AR10, 1000 km³
(b)
H2O saturated
3 wt.% H2O
2 wt.% H2O
0.6
0.2
Maximum segregation timescales
Time (kyr)

821

822

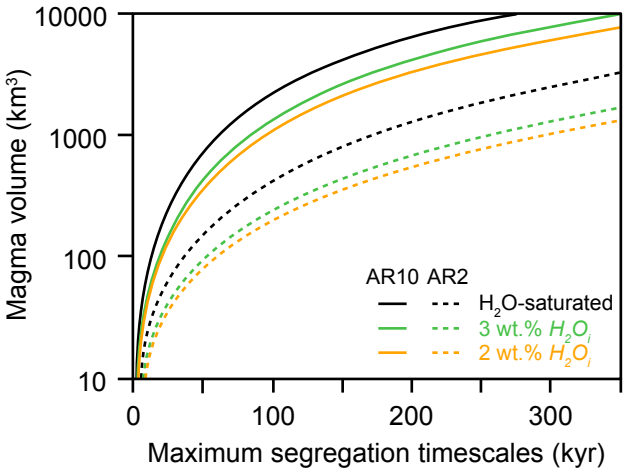
10000
1000
100
10
Magma volume (km³)
0
100
200
300
Maximum segregation timescales (kyr)
AR10 AR2
H2O-saturated
3 wt.% H2Oi
2 wt.% H2Oi

823

824

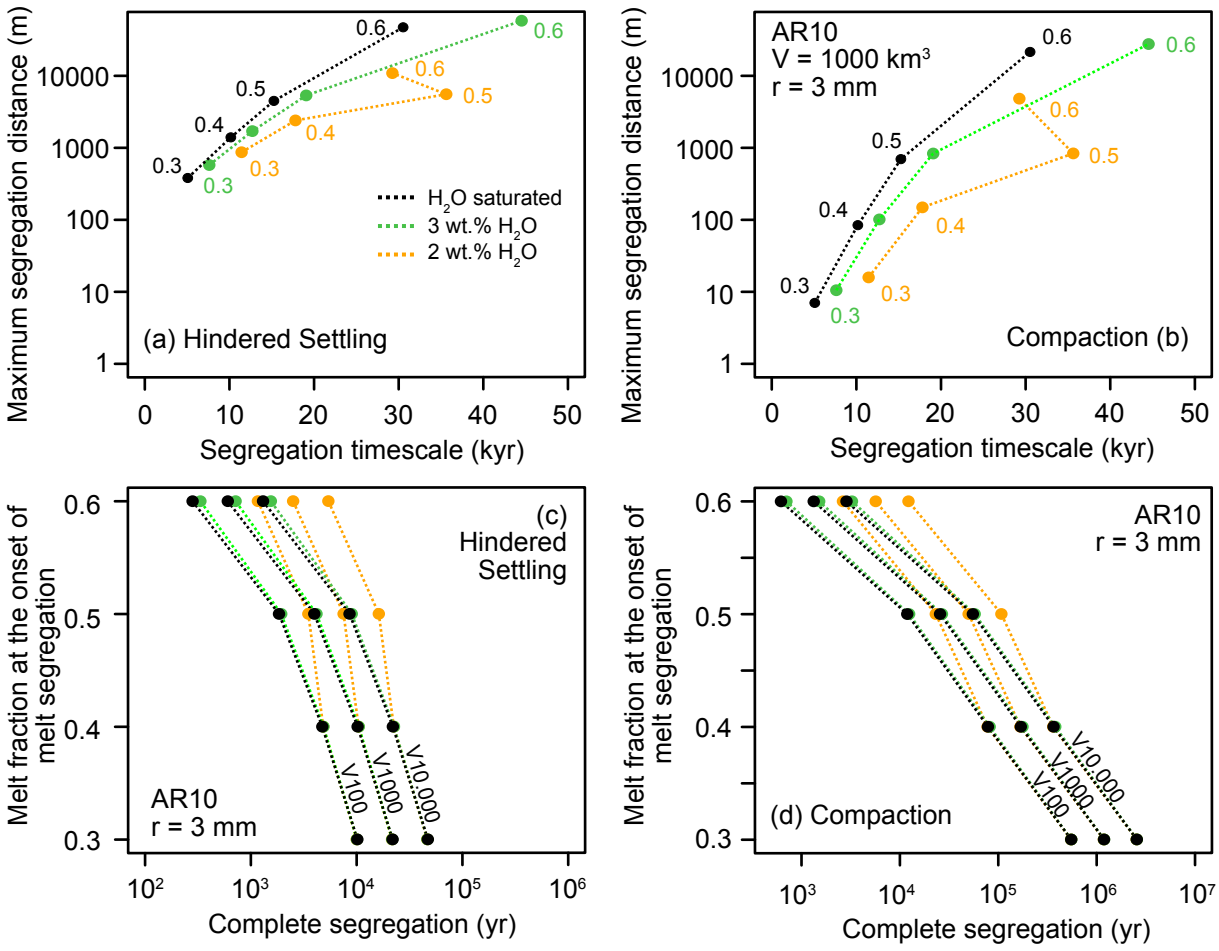
Maximum segregation distance (m)
Segregation timescale (kyr)
(a) Hindered Settling
H2O saturated
3 wt.% H2O
2 wt.% H2O
AR10
V = 1000 km3
r = 3 mm
Compaction (b)
Melt fraction at the onset of melt segregation
Complete segregation (yr)
(c) Hindered Settling
AR10
r = 3 mm
V100
V1000
V10,000
(d) Compaction

825

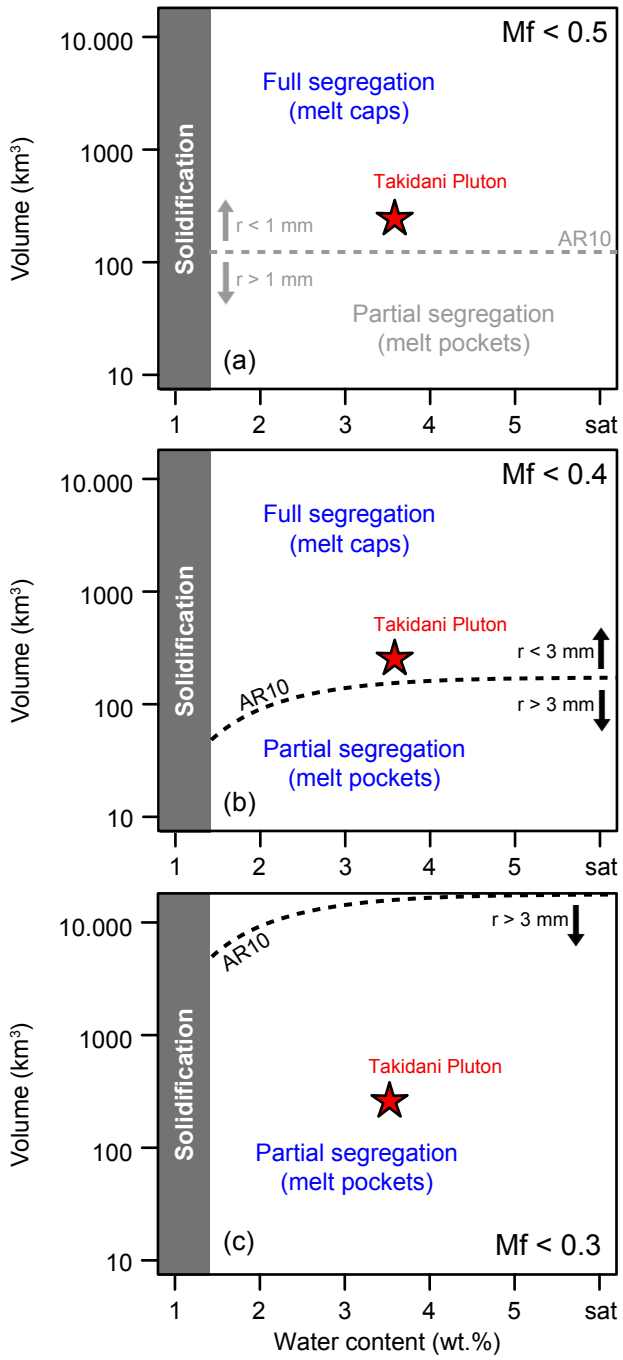
Mf < 0.5
Full segregation
(melt caps)
Takidani Pluton
r < 1 mm
AR10
r > 1 mm
Partial segregation
(melt pockets)
(a)
Solidification
Volume (km³)
10.000
1000
100
10
1
2
3
4
5
sat
Mf < 0.4
Full segregation
(melt caps)
Takidani Pluton
r < 3 mm
AR10
r > 3 mm
Partial segregation
(melt pockets)
(b)
Mf < 0.3
(c)
Water content (wt.%)

826

827

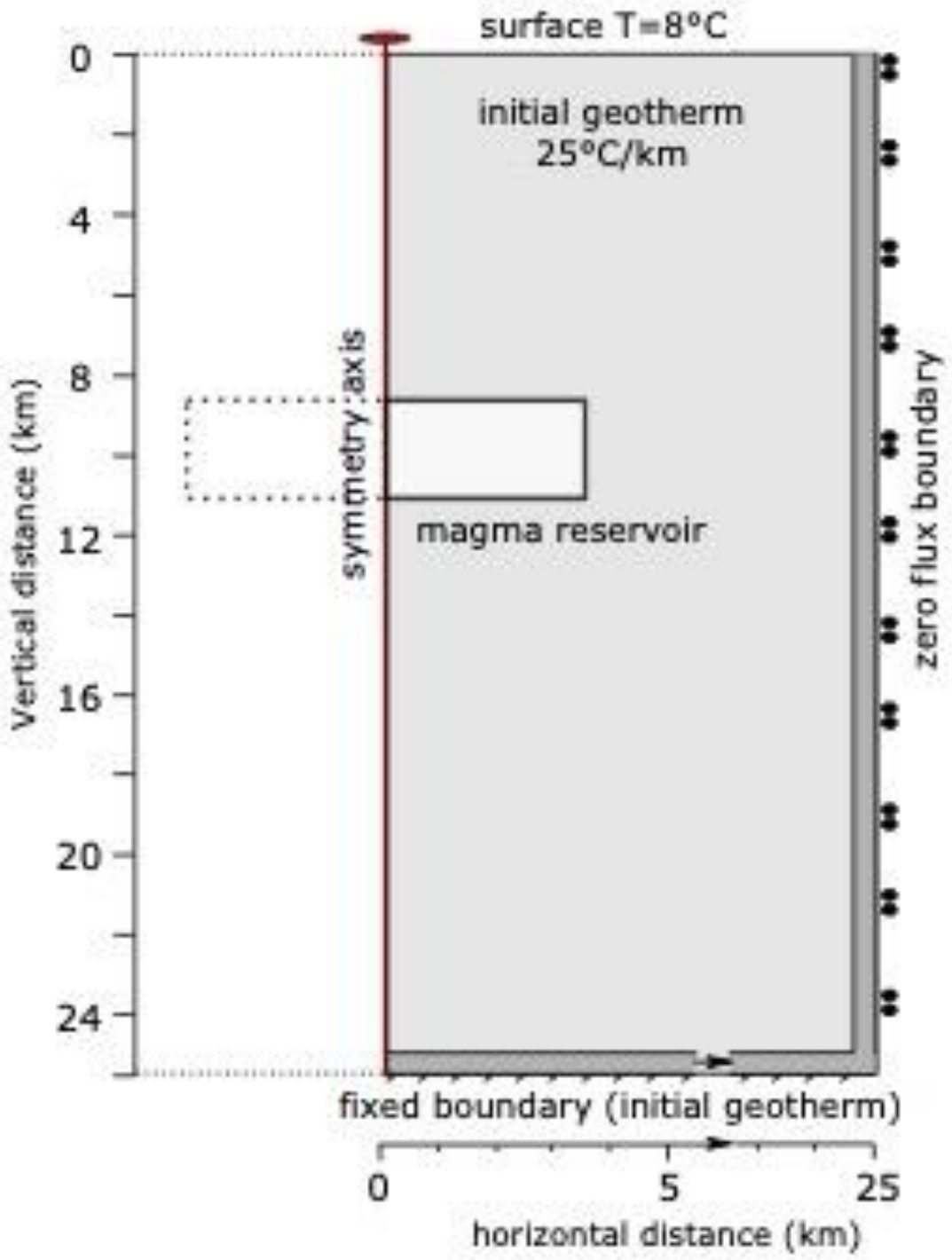

Figure S1:
Geometry of the axisymmetric thermal model. Instantaneous intrusion of a cylindrical magma reservoir at 10 km depth is modelled for magma volumes of 100, 1000 and 10.000 km^3. The surface temperature is fixed at 8°C and the initial geothermal gradient is set to 25°C/km. Upper and lower boundaries are fixed temperature, while a zero flux condition is imposed on the right boundary. The left boundary of the model is the plane of symmetry.

Table 1

Interstitial melt components from QEMSCAN and EMPA

1) Mineral abundance (QEMSCAN, normalised to 100)

Number	Sample	Qtz	Kfs	Plg<An30
1	EH16	26.1	14.6	11.7
2	EH23	21.4	14.3	14.1
3	EH12	26.5	15.6	15.3
4	EH76	28.5	19	15.9
5	EH70	31.1	21.9	15.2

2) Interstitial melt composition (Calculated using EMPA)

Number	Sample	Qtz	Or	Ab
1	EH16	0.5 (±0.01)	0.25 (±0.02)	0.25 (±0.04)
2	EH23	0.43 (±0.01)	0.27 (±0.03)	0.3 (±0.05)
3	EH12	0.46 (±0.01)	0.25 (±0.03)	0.29 (±0.06)
4	EH76	0.45 (±0.01)	0.28 (±0.04)	0.27 (±0.07)
5	EH70	0.46 (±0.01)	0.29 (±0.03)	0.25 (±0.07)

Sample location are presented in Hartung et al. (2017)

Table 2

List of parameters used in thermal modelling.

Specific heat	1000 $J\ kg^{-1}\ K^{-1}$
Thermal conductivity	as in Whittington et al., (2009)
Latent heat	3.13×10^5 $J\ kg^{-1}$
Density (melt and solid)	2700 $kg\ m^{-3}$
Initial geothermal gradient	25 $^oC\ km^{-1}$
Surface temperature	8 ^oC
Intrusion depth	10 km
Intrusion volumes	100, 1000, 10.000 km^3

Table 3

Polynomial fits (Figure 8)

1) Aspect ratio 10	
H_2O-saturated	$y = -3E\text{-}13x^3 + 2E\text{-}07x^2 + 0.0053x + 0.9947$
3 wt.% H_2O_i	$y = -1E\text{-}13x^3 + 1E\text{-}07x^2 + 0.0033x + 0.9967$
2 wt.% H_2O_i	$y = -1E\text{-}13x^3 + 9E\text{-}08x^2 + 0.0031x + 0.9969$
2) Aspect ratio 2	
H_2O-saturated	$y = 2E\text{-}08x^2 + 0.002x + 0.998$
3 wt.% H_2O_i	$y = 1E\text{-}08x^2 + 0.0014x + 0.9986$
2 wt.% H_2O_i	$y = 8E\text{-}09x^2 + 0.0012x + 0.9988$